Supporting Information

Chemical composition control at the substrate interface as the key for FeSe thin film growth

Yukiko Obata[1], Michiko Sato[2], Yuji Kondo[2], Yuta Yamaguchi[3], Igor A. Karateev[4], Ivan Pavlov[5], Alexander L. Vasiliev[4,5,6,*], Silvia Haindl[1*]*

[1]Tokyo Tech World Research Hub Initiative (WRHI), Institute of Innovative Research, Tokyo Institute of Technology, 4259 Nagatsuta-cho, Midori-ku, Yokohama, Kanagawa 226-8503, Japan

[2]Materials Research Center for Element Strategy, Tokyo Institute of Technology, 4259 Nagatsuta-cho, Midori-ku, Yokohama, Kanagawa 226-8503, Japan

[3]Laboratory for Materials and Structures, Institute of Innovative Research, Tokyo Institute of Technology, 4259 Nagatsuta-cho, Midori-ku, Yokohama, Kanagawa 226-8503, Japan

[4]National Research Centre "Kurchatov Institute," pl. Akademika Kurchatova 1, Moscow, 123182, Russian Federation

[5]Shubnikov Institute of Crystallography of FSRC “Crystallography and Photonics” Russian Academy of Sciences, Leninsky pr. 59, Moscow, 119333, Russian Federation

[6]Moscow Institute of Physics and Technology, National Research University, Dolgoprudny, Moscow region 141701, Russian Federation

Corresponding authors:

*Yukiko Obata: obata.y.ab@m.titech.ac.jp

*Alexander Vasiliev: a.vasiliev56@gmail.com

*Silvia Haindl: haindl.s.aa@m.titech.ac.jp

Changes in FeSe Target Composition and Target Surface Roughness. The change from a nearly stoichiometric FeSe target to a noticeably Se-deficient one upon laser irradiation resulted in a reduced reproducibility of the crystalline FeSe phase. Fig. S1(a) shows a comparison of 2θ/ω scans between two FeSe/MgO films fabricated using comparable parameters (T_S = 500ºC; rep. rate = 10 Hz) from a fresh and an altered target surface (after the growth of 10 more films), demonstrating the change from a purely *c*-axis oriented, tetragonal FeSe to a film with FeSe (101) orientated grains and secondary phases such as hexagonal FeSe (*h*-FeSe). Figs. S1(b),(c) show compositional images of the FeSe target surface before and after the growth of ~30 films. The target surface had become severely rough and spiky after laser irradiation. The analysis of the target composition by EPMA shows a strong Se loss and illustrates the difficulty of maintaining the control of chemical homogeneity and reproducibility in PLD of several films.

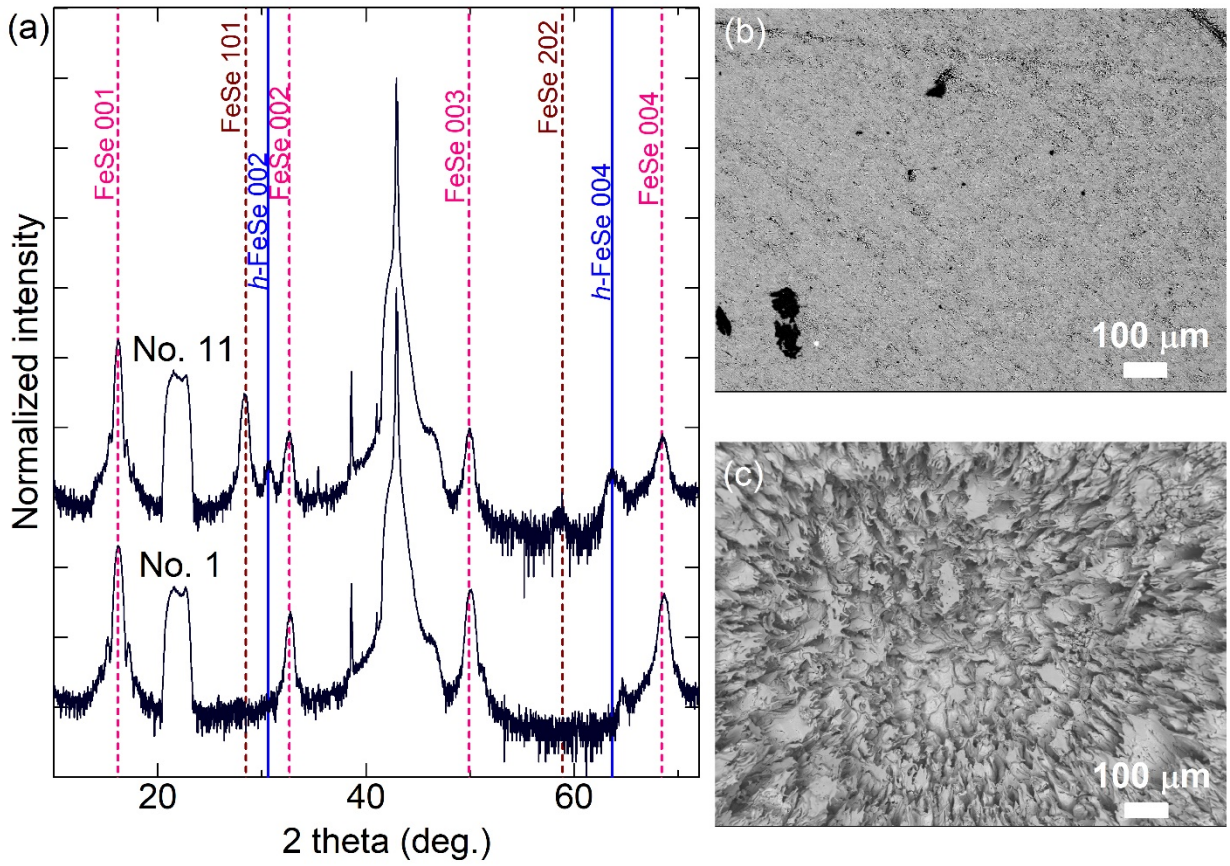

Figure S1. (a) Comparison between the 2θ/ω scan (denoted as "No. 1") of the FeSe/MgO film (T_S = 500ºC; rep. rate = 10 Hz) and that (denoted as "No. 11") of the film fabricated at the same condition after the growth of 10 films. **(b), (c)** Compositional images of the FeSe target surface obtained by EPMA before and after the growth of ~30 films.

Structural Characterization of the FeSe/MgO Films Deposited at 2 Hz. A similar temperature dependence of the crystalline FeSe phase was found in the FeSe/MgO films deposited at 2 Hz. Fig. S2(a) shows, exemplarily, 2θ/ω XRD scans for the FeSe/MgO films deposited at different T_S = 220 – 500ºC, and illustrates the growth of a *c*-axis oriented, tetragonal FeSe film at T_S = 260 – 400ºC (pink shaded region). At lower T_S (220°C), FeSe(110) reflections appeared, whereas

FeSe(101) as well as hexagonal, *h*-FeSe(001), was detected at higher T_S (500°C). Subsequently, the relative *in-plane* orientations were studied for selected films in pole figure measurements based on FeSe(101) and MgO(222) reflections. Similar to the texture found in the FeSe/MgO films deposited at 10 Hz, the FeSe(101) pole figures in Figs. S2(c) – (f) reveal that the films grew with two different *in-plane* textures: the majority of grains is oriented [100]FeSe//[100]MgO (*cube-on-cube*), whereas a minority shows a [100]FeSe//[110]MgO texture (45º *in-plane* rotation with respect to the majority). An exception was observed in the film grown at 500ºC (Fig. S2(g)), where much more complex texture was detected due to the impurity phases.

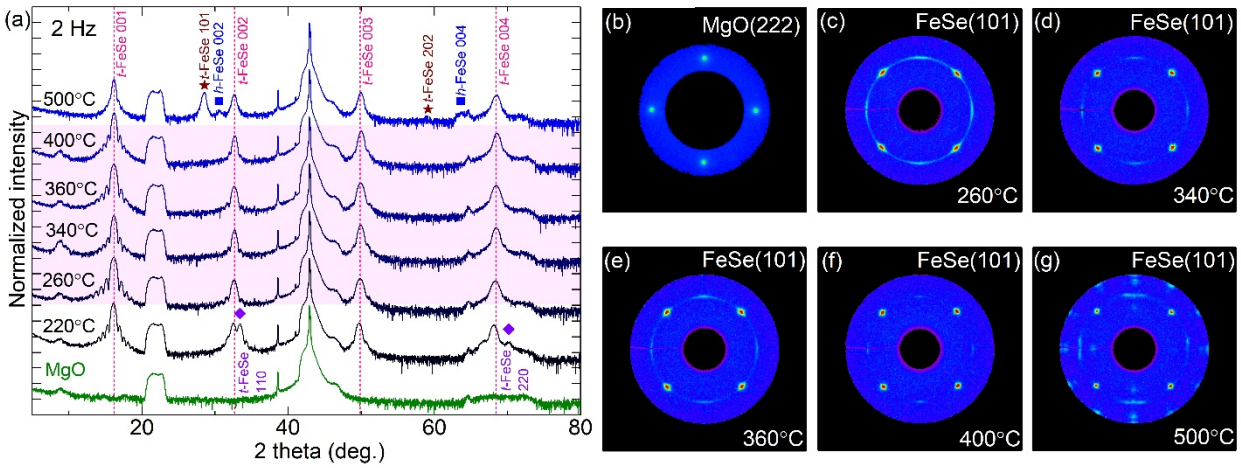

Figure S2. XRD results for FeSe/MgO films deposited at 2 Hz: **(a)** 2θ/ω scans of films and MgO reference (logarithmic scale). Intensities were normalized with respect to the MgO (002) reflection. The pink shaded region shows the *c*-axis oriented FeSe films. **(b)** (222) pole figure of MgO. **(c) – (g)** (101) pole figures of FeSe/MgO grown at 260, 340, 360, 400, and 500ºC.

Surface Morphology Analysis. Changes in surface morphology of the FeSe/MgO films grown at the repetition rates of 2 and 10 Hz are demonstrated in AFM images depicted in Figs. S3(a) – (l). These results imply that there is a stronger tendency in the films grown at 2 Hz compared to those deposited at 10 Hz for a pronounced island growth mode as the substrate temperatures rise.

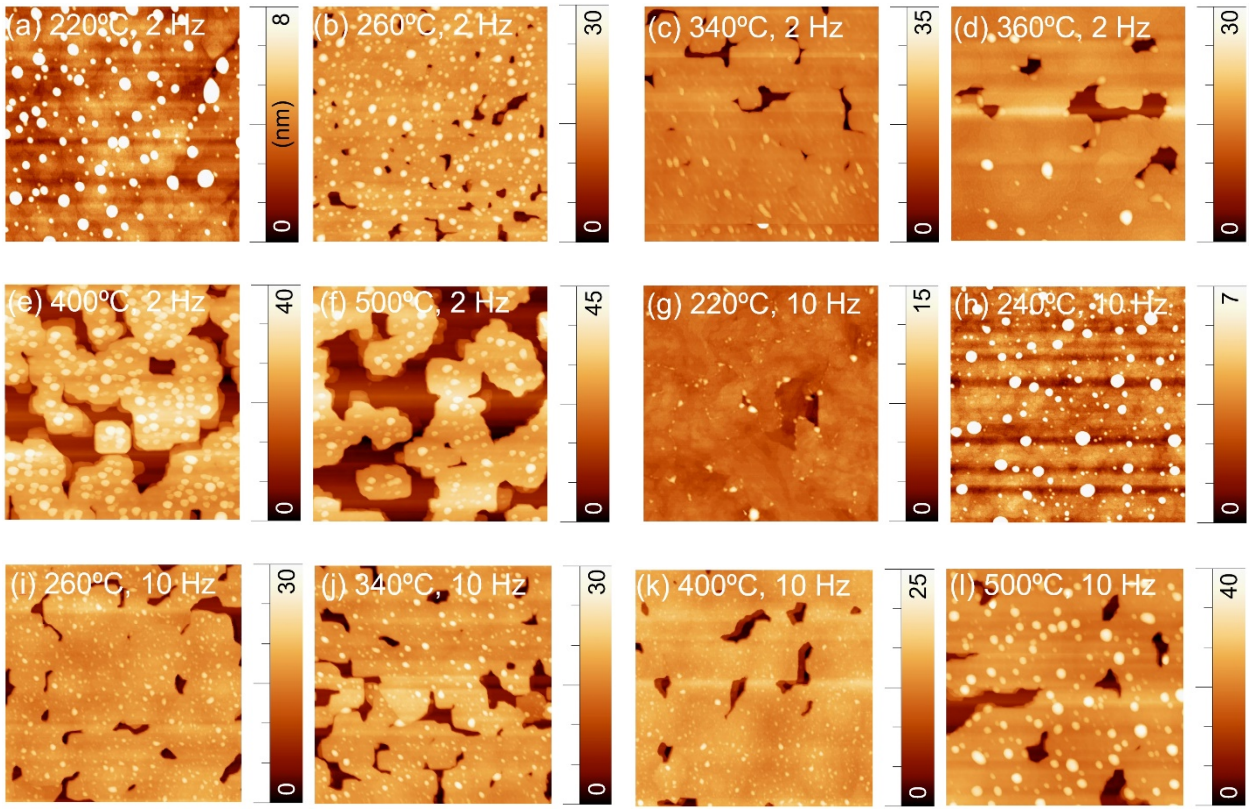

Figure S3. (a) – (f) AFM images of the FeSe/MgO films grown at T_S = 220, 260, 340, 360, 400, and 500ºC with 2 Hz. **(g) – (l)** Those at T_S = 220, 240, 260, 340, 400, and 500ºC with 10 Hz. All the images were captured on an area of 1 × 1 μm^2.

Electrical Transport Properties. The electrical characterization of the FeSe/MgO films with thicknesses in the range of 10 – 20 nm agrees with previously reported results of a suppressed superconductivity:[1] all of the films showed a semiconducting-like behavior of their resistivities, and none of the films exhibited superconductivity down to 2 K (blue-yellow region in Fig. S4a(a)). Even an additional *in-situ* post annealing for 30 minutes at various temperatures of films prepared at 350ºC did not result in a superconducting transition (green region in Fig. S4a(a)). We also evaluated Sheet resistance, $R_{\square} = Rwt/lc$, where R, w, t, l, and c represent the measured resistance, width, film thickness, length, and c-axis lattice parameter, respectively. Fig. S4a(b) shows the temperature dependence of $R_{\square}$ for the corresponding films illustrated in Fig. S4a(a), revealing that all of them mainly stay in the insulating region, which has been previously reported to be separated from the superconducting region of FeSe with the quantum resistance represented by the von-Klitzing constant, $R_K = h/e^2$ (h: Planck constant, e: elementary charge).[2] With increasing post-annealing temperatures, $R_{\square}$ was found to gradually approach R_K, suggesting the possibility of inducing superconductivity by post-annealing at higher temperatures. However, this seems hardly feasible due to an increase in Se evaporation at elevated temperatures, which inevitably leads to further chemical inhomogeneity in the films.

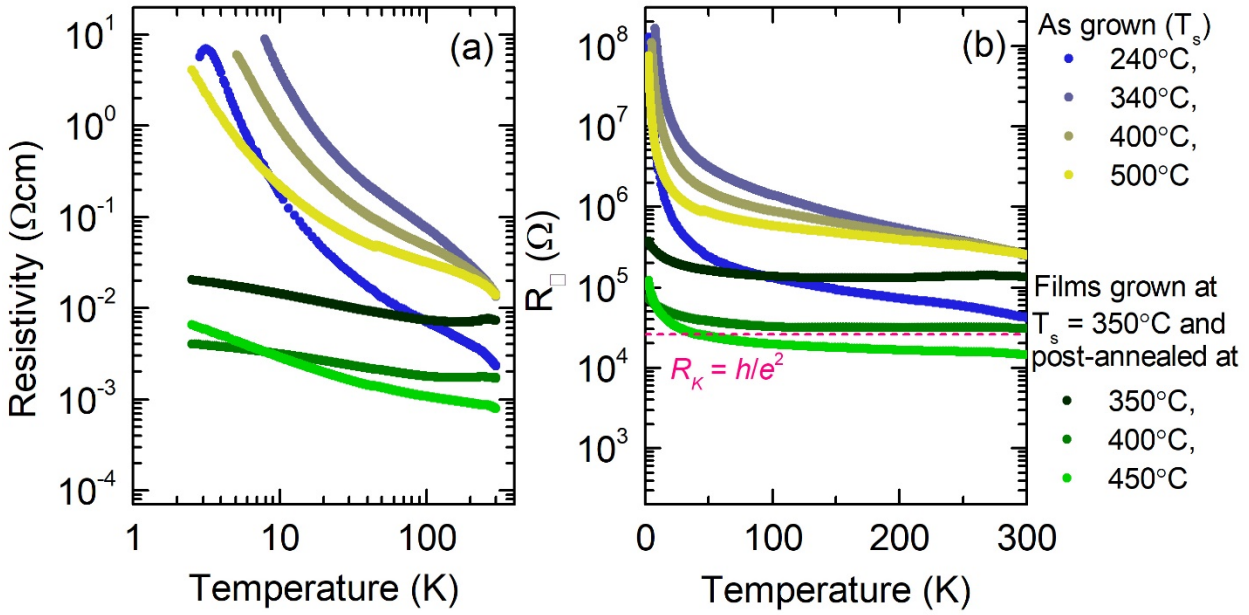

Figure S4a. (a) Resistivity and **(b)** Sheet resistance, $R_{\square}$, vs. temperature curves for the as-grown FeSe/MgO films deposited at various T_S (blue-yellow region) and those grown at 350ºC and subsequently post-annealed at various different temperatures for 30 min (green region). The pink dot line represents the von-Klitzing constant, $R_K = h/e^2$ (h: Planck constant, e: elementary charge).

Compositional Analysis along the Film Cross Section. Figure S5 shows the HAADF-STEM image and cross-sectional individual maps for single elements (Fe, Se, Mg, O, and Pt) of the 15 nm thin FeSe/MgO film (T_S = 400ºC; rep. rate = 10 Hz). The film was later covered by a 50 nm thin Pt cap layer to prevent it from further oxidation. A ~1 nm thin Fe-rich layer was found at the film/substrate interface with an additional influence on the local strain distribution. Fe diffusion into the substrate takes place. Furthermore, a ~3 nm thin Fe-rich (or Se deficient layer) was confirmed at the top of the film. The top part of the film (~2 nm) shows signatures of an oxidation layer (that formed before Pt capping). In total, an inhomogeneous composition distribution of Fe

and Se can be found along the film cross section with Fe-rich zones at the film/substrate interface and close to the film surface.

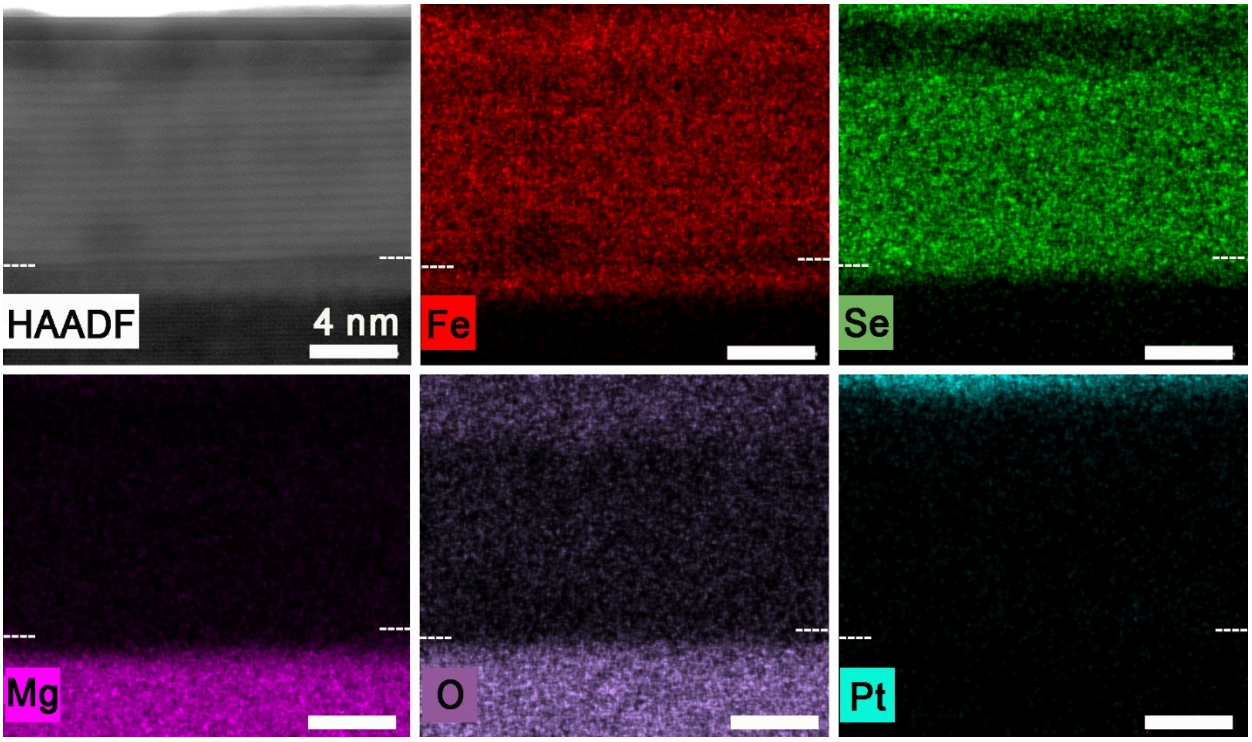

Figure S5. HAADF-STEM image and cross-sectional individual maps for single elements (Fe, Mg, O, Pt, and Se) of the 15 nm thin FeSe/MgO film (T_S = 400ºC; rep. rate = 10 Hz). White markers indicate the top of the substrate.

Next figures show the compositional analysis of film surface (Figure S6), film/substrate interface (Figure S7) with an Fe diffusion zone within the substrate, and domain-matching epitaxy of FeSe/MgO films (Figure S8).

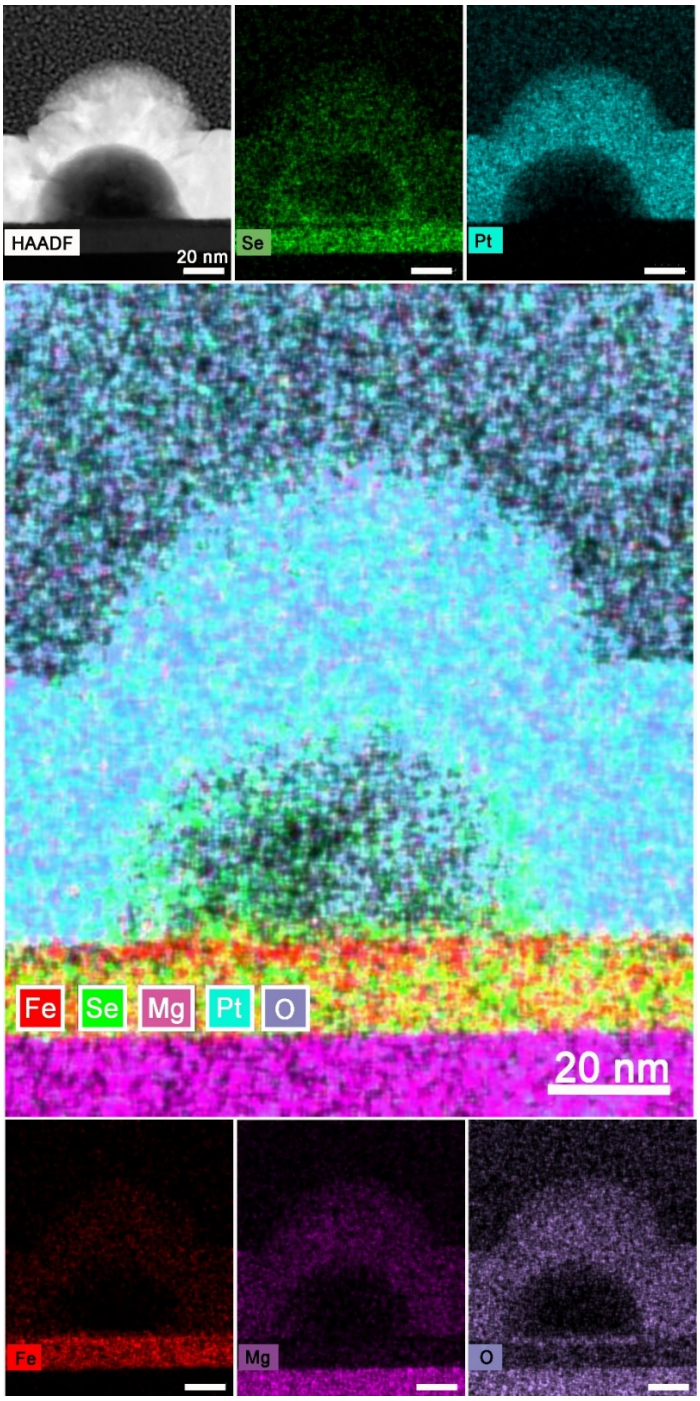

Figure S6. HAADF-STEM images and cross-sectional individual maps for single elements (Fe, Mg, O, Pt, and Se) of the FeSe/MgO film (T_S = 400ºC; rep. rate = 10 Hz) surface with Se-rich precipitate that reacted and grew in air. These are typical artifacts on the surface. Scale bares are 20 nm.

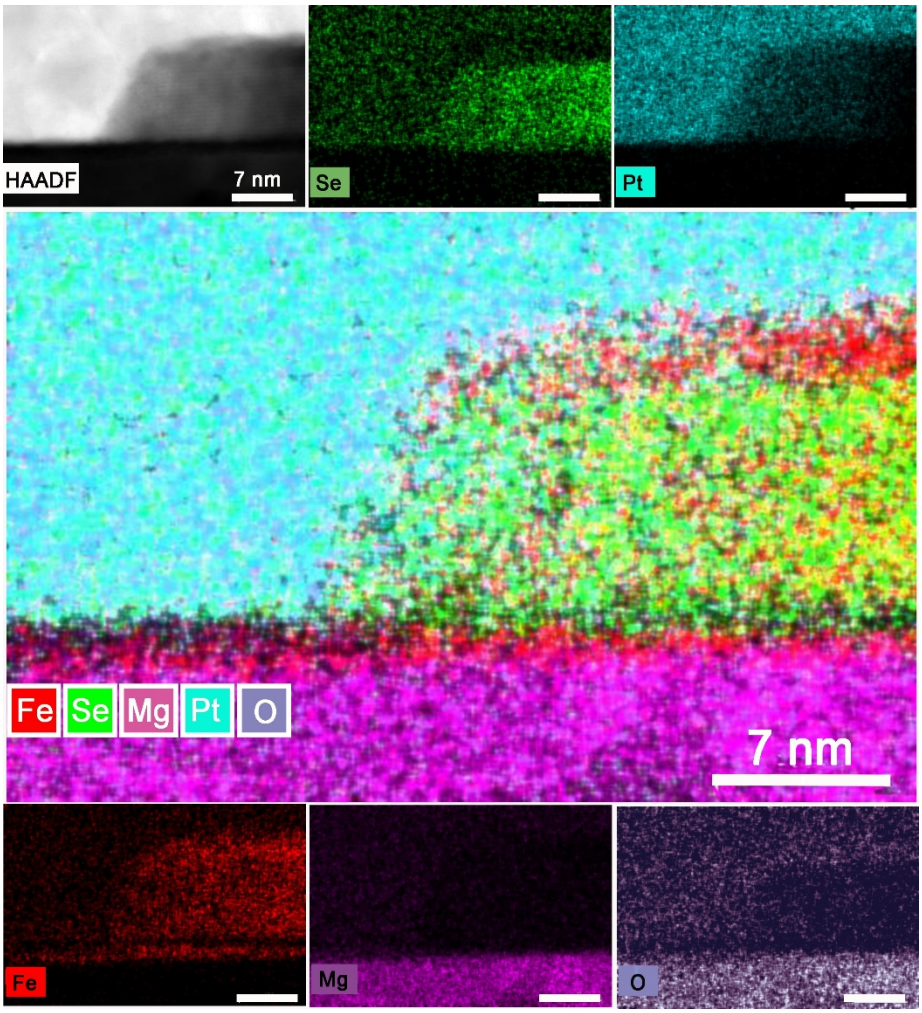

Figure S7. HAADF-STEM images and cross-sectional individual maps for single elements (Fe, Mg, O, Pt, and Se) of an FeSe island and its vicinity (T_S = 400ºC; rep. rate = 10 Hz) in the FeSe/MgO film. Note that Fe diffusion into MgO appears below and between FeSe islands. Scale bars are 7 nm.

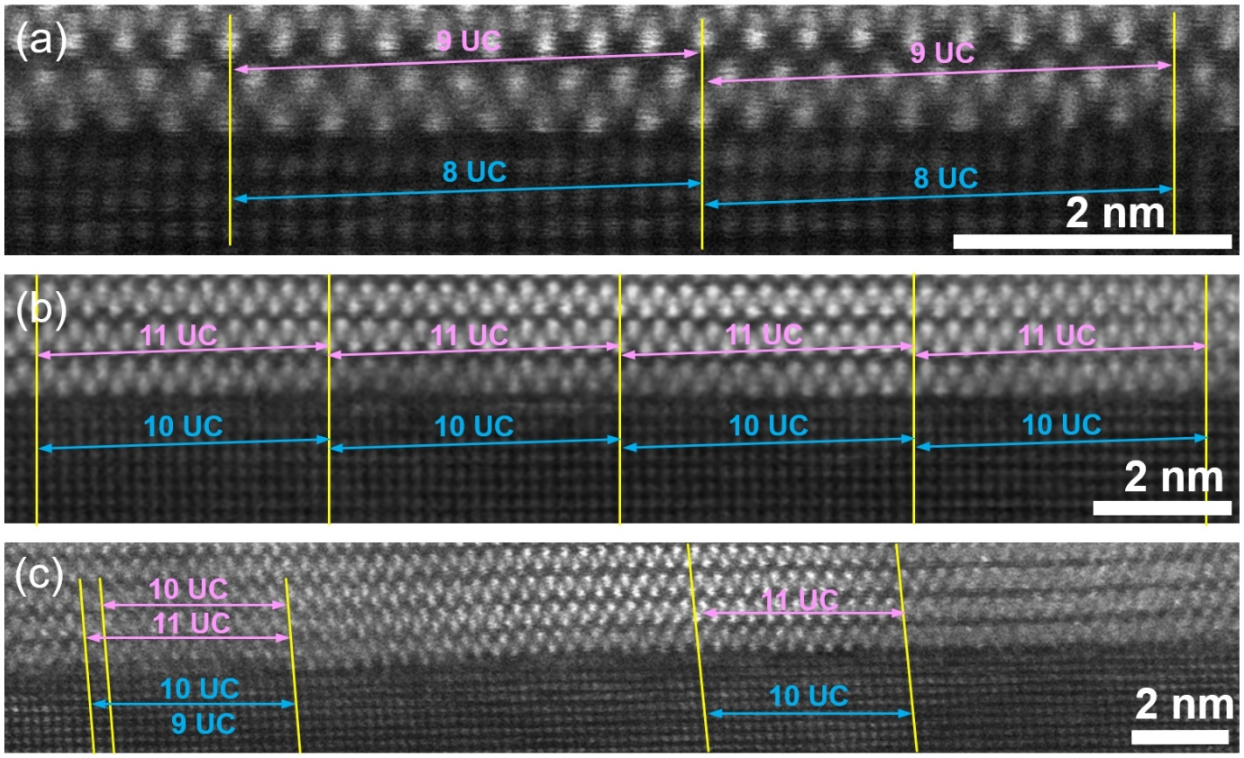

Figure S8. (a) - (c) HAADF-STEM images of the FeSe/MgO interface. Yellow lines indicate matching domains of FeSe and MgO unit cells. Film parameters are 500°C, 10 Hz (t = 17 nm).

AES Depth Profile Analysis. AES depth profiling confirms the chemical inhomogeneities along the film cross section of a 31 nm-thin FeSe/MgO film grown at 350ºC with 10 Hz. The calculated chemical composition with depth (increasing sputtering time) is displayed in Fig. S9(a) and indicates the variation of atomic concentrations of Fe (red), Se (light green), Mg (black), and O (blue). In this example, the gradient of O concentration is broader compared to that shown in the TEM-EDXS elemental mapping (Fig. 4(b)) or in comparable thicker films, and results from the island-like morphology and several observed cracks in the film. Nevertheless, it is clear that a Fe:Se ratio close to 1:1 is only reached in 2/3 of the film cross section, while top regions and the film/substrate interface are Se-deficient. The corresponding first derivatives of AES spectra are shown for selected sputtering times in Fig. S9(b). At a sputtering time of 13 min the Mg KLL transitions appear and indicate the FeSe/MgO interface. Fe LMM intensities remain almost constant across the film, whereas those for Se LMM become weak towards the top surface and the film/substrate interface. We point out that the quality of the films analyzed by TEM-EDXS and AES is comparable.

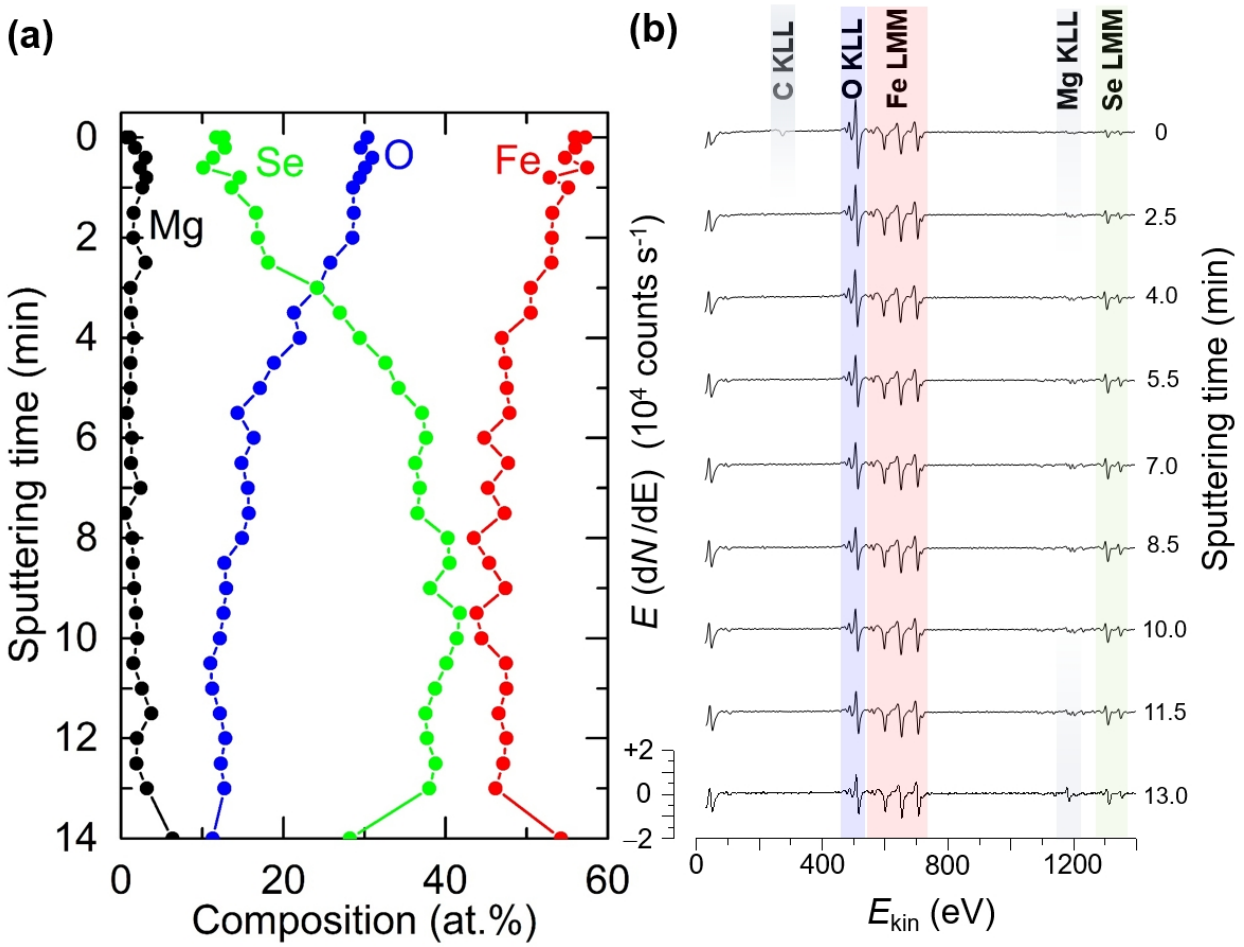

Figure S9. (a) AES depth profile and **(b)** derivatives of AES spectra at selected sputtering times of a 31 nm thin FeSe/MgO film (T_S = 350ºC; rep. rate = 10 Hz). The gradient of oxygen concentration with respect to depth in AES depth profile is broader than that in the TEM-EDXS elemental mapping, suggesting the larger distribution of FeSe islands which inevitably results in an increase in surface area of the film exposed to air. The films analyzed by TEM-EDXS and AES are qualitatively comparable to each other. Some of the AES depth profiles measured at different positions in the same sample show more Fe-rich concentration along the film cross-section compared to the selected example here.

Implications for other Fe-chalcogenide Thin Films (i.e. $FeSe_{1-x}Te_x$). The control of the film/substrate interface for film textures and superconducting properties is also crucial in other Fe-chalcogenide superconducting films grown on MgO substrates, such as $FeSe_{1-x}Te_x$. At least, a consistent picture on texture evolution can be found for various physical vapor deposition methods, like PLD, MBE or radio-frequency (rf) sputtered films.[3] Two texture domains were reported by Chang *et al.*,[4] and from several studies,[3,5,6] one can attribute to the substrate temperature a dominant effect in controlling the film textures: the general observation includes a change from a single texture component with [100](001)$FeSe_{0.5}Te_{0.5}$//[110](001)MgO at low substrate temperatures (~280°C) into a mixture of [100](001)$FeSe_{0.5}Te_{0.5}$//[100](001)MgO and [100](001)$FeSe_{0.5}Te_{0.5}$//[110](001)MgO at 400ºC and finally a single *cube-on-cube* texture for films grown at ~500ºC. The structural parameters of the deposited films on MgO are, however, in most cases not favorable for superconductivity, and increasing substrate temperatures were found to gradually suppress superconductivity and eventually produce semiconducting films.[5] Based on equivalent results, Molatta *et al.* have improved control and reproducibility in the growth of superconducting $FeSe_{1-x}Te_x$ films. By using non-superconducting $FeSe_{1-x}Te_x$ seed layer with excellent *cube-on-cube* epitaxy, the subsequent homoepitaxial growth of $FeSe_{1-x}Te_x$ films could be achieved at reduced T_S = 200 – 340°C.[6] For FeTe films, the film texture on MgO(100) looks to be again more complex: Shchichko *et al.*[7] reported several epitaxial relations for FeTe thin films grown at 400ºC: a single orientation of (001)[110]FeTe//(001)[110]MgO was found in one film, whereas another film two different domains with orientations (01-1)[111]FeTe//(001)[110]MgO and (001)[010]FeTe//(001)[110]MgO occurred. The use of an Fe-buffer layer in PLD of $FeSe_{1-x}Te_x$ films has apparently improved epitaxial growth.[8]

Diverse Interfaces of Fe-chalcogenide Thin Films on Different Substrates. Various TEM studies on Fe-chalcogenide thin film interfaces are summarized in the Chapter 4 of Ref. [9]. Many studies show a blurred interfacial region and only a few studies have atomically resolved the interface between FeSe thin film and substrates. For FeSe/CaF_2, a previous TEM report has noted interfacial reaction with the formation of CaSe.[10] This is in sharp contrast to the interface between Fe chalcogenide and STO, which is Se/Te-rich, as illustrated by Zhu *et al*. in their STEM studies on the PLD-grown $FeSe_{1-x}Te_x$/STO heterointerface.[11] In case of monolayer FeSe/STO, interface structure further varies with different conditions such as substrate pre-treatment and substrate surface termination as well as with deposition method,[9,12,13] imposing a challenge for developing a unified picture.

Despite this difficulty in resolving the atomic structure of the interfaces, LME can be expected in Fe chalcogenide thin films on STO and other substrates such as LAO and LSAT due to the much smaller initial misfit strain compared to that in MgO. In Zhu *et al*. ,[11] a misfit dislocation layer at the interface was reported. Our inspection of the STEM image reveals a domain-matching ratio of m_{FST}/n_{STO} = 30/29, which slightly deviates from the theoretical estimate of 36/35 (ε = 2.9 %, $a_{FST\ bulk}$ = 3.793 Å and a_{STO} = 3.905 Å).

REFERENCES

(1) Wu, M. K.; Hsu, F. C.; Yeh, K. W.; Huang, T. W.; Luo, J. Y.; Wang, M. J.; Chang, H. H.; Chen, T. K.; Rao, S. M.; Mok, B. H.; Chen, C. L.; Huang, Y. L.; Ke, C. T.; Wu, P. M.; Chang, A. M.; Wu, C. T.; Perng, T. P. The Development of the Superconducting PbO-Type β-FeSe and Related Compounds. *Physica C: Superconductivity* **2009**, *469* (9), 340–349.

(2) Schneider, R.; Zaitsev, A. G.; Fuchs, D.; v. Löhneysen, H. Superconductor-Insulator Quantum Phase Transition in Disordered FeSe Thin Films. *Phys. Rev. Lett.* **2012**, *108* (25), 257003.

(3) Mousavi, T.; Grovenor, C.; Speller, S. Characterization of Superconducting $Fe_y(Se_{1-x}Te_x)$ Thin Films Deposited on MgO Substrates by Sputtering. *J Mater Sci* **2015**, *50* (21), 6970–6978.

(4) Chang, H. H.; Luo, J. Y.; Wu, C. T.; Hsu, F. C.; Huang, T. W.; Wu, P. M.; Wu, M. K.; Wang, M. J. The Vortex State of $FeSe_{1-x}Te_x$ Superconducting Thin Films. *Supercond. Sci. Technol.* **2011**, *24* (10), 105011.

(5) Huang, S. X.; Chien, C. L.; Thampy, V.; Broholm, C. Control of Tetrahedral Coordination and Superconductivity in $FeSe_{0.5}Te_{0.5}$ Thin Films. *Phys. Rev. Lett.* **2010**, *104* (21), 217002.

(6) Molatta, S.; Haindl, S.; Trommler, S.; Schulze, M.; Wurmehl, S.; Hühne, R. Interface Control by Homoepitaxial Growth in Pulsed Laser Deposited Iron Chalcogenide Thin Films. *Sci Rep* **2015**, *5* (1), 1–7.

(7) Shchichko, I. O.; Presnyakov, M. Y.; Stepantsov, E. A.; Kazakov, S. M.; Antipov, E. V.; Makarova, I. P.; Vasil'ev, A. L. Electron Microscopy of Iron Chalcogenide FeTe(Se) Films. *Crystallogr. Rep.* **2015**, *60* (3), 370–376.

(8) Iida, K.; Hänisch, J.; Schulze, M.; Aswartham, S.; Wurmehl, S.; Büchner, B.; Schultz, L.;

Holzapfel, B. Generic Fe Buffer Layers for Fe-Based Superconductors: Epitaxial $FeSe_{1-x}Te_x$ Thin Films. *Applied Physics Letters* **2011**, *99* (20), 202503.

(9) Haindl, S. *Iron-Based Superconducting Thin Films*, 1st ed. 2021 edition.; Springer, 2021.

(10) Qiu, W.; Ma, Z.; Patel, D.; Sang, L.; Cai, C.; Shahriar Al Hossain, M.; Cheng, Z.; Wang, X.; Dou, S. X. The Interface Structure of FeSe Thin Film on CaF_2 Substrate and Its Influence on the Superconducting Performance. *ACS Appl. Mater. Interfaces* **2017**, *9* (42), 37446–37453.

(11) Zhu, Y.; Chen, L.; Ciston, J.; Wang, H. Atomic-Scale Investigations of Intrinsic Chemical Inhomogeneity in Superconducting $Fe_{1+y}Se_{1-x}Te_x$ Epitaxial Films. *J. Phys. Chem. C* **2013**, *117* (14), 7170–7177.

(12) Li, F.; Ding, H.; Tang, C.; Peng, J.; Zhang, Q.; Zhang, W.; Zhou, G.; Zhang, D.; Song, C.-L.; He, K.; Ji, S.; Chen, X.; Gu, L.; Wang, L.; Ma, X.-C.; Xue, Q.-K. Interface-Enhanced High-Temperature Superconductivity in Single-Unit-Cell $FeTe_{1-x}Se_x$ Films on $SrTiO_3$. *Phys. Rev. B* **2015**, *91* (22), 220503.

(13) Zhao, W.; Li, M.; Chang, C.-Z.; Jiang, J.; Wu, L.; Liu, C.; Moodera, J. S.; Zhu, Y.; Chan, M. H. W. Direct Imaging of Electron Transfer and Its Influence on Superconducting Pairing at FeSe/$SrTiO_3$ Interface. *Science Advances* **2018**, *4* (3), eaao2682.